A&A 537, A22 (2012)
DOI: 10.1051/0004-6361/201117926

Astronomy & Astrophysics

Atomic data for the X-ray lines of Fe VIII and Fe IX⋆

B. O'Dwyer[1], G. Del Zanna[1], N. R. Badnell[2], H. E. Mason[1], and P. J. Storey[3]

[1] DAMTP, Centre for Mathematical Sciences, Wilberforce Road, Cambridge CB3 0WA, UK
e-mail: b.o-dwyer@damtp.cam.ac.uk
[2] Department of Physics, University of Strathclyde, Glasgow G4 0NG, UK
[3] Department of Physics and Astronomy, University College London, Gower Street, London WC1E 6BT, UK

Received 22 August 2011 / Accepted 19 September 2011

ABSTRACT

The distorted wave extension of the AUTOSTRUCTURE code has been used to calculate energy levels, radiative transition probabilities and collisional excitation rates of Fe VIII and Fe IX up to $n = 6$ for Fe IX and $n = 7$ for Fe VIII. We have compared some of the data with previous calculations, finding overall agreement for radiative transition rates, but interesting differences for some collisional data. We have merged our data for the higher energy levels with published R-matrix collisional excitation rates for the lower ones to calculate spectral line intensities and compare them with observations. In particular, we have focused on the transitions from high energy levels of Fe VIII & Fe IX which are present in the 93–95 Å region. A few new identifications are tentatively provided. We find that Fe IX 5f–3d and Fe VIII 7f–3d transitions only comprise a small fraction of the observed lines in the 93–95 Å region for quiet Sun conditions, and thus their contribution to the Solar Dynamics Observatory (SDO) Atmospheric Imaging Assembly (AIA) 94 Å band is expected to be small.

Key words. atomic data – line: identification – techniques: spectroscopic

1. Introduction

The 50–170 Å spectral region is dominated by a forest of transitions, many of which are from $n = 4, 5, 6$ and 7 states of highly ionised iron ions, and for which little atomic data are available (see Fawcett et al. 1968; Jordan 1968). This spectral region has been observed with various solar instruments on-board sounding rockets, and more recently with *Chandra* LETG (see Brinkman et al. 2000) and the Solar Dynamics Observatory (SDO). SDO has been providing new extreme-ultraviolet (EUV) observations of the Sun, at unprecedented cadence. One of the instruments, the Atmospheric Imaging Assembly (AIA, see Lemen et al. 2011) has been providing narrow-band EUV images at various wavelengths, centred at 94, 131, 171, 193, 211, and 335 Å. The relevant atomic data for the spectral lines contributing to some of these bands are relatively well understood, however a significant amount of data is still lacking. See O'Dwyer et al. (2010) and Del Zanna et al. (2011) for details.

This work is in part motivated by the desire to determine the contribution of transitions from high energy levels of Fe VIII & Fe IX to the SDO AIA 94 Å band. The work of Aschwanden & Boerner (2011) has hinted at the presence of missing flux at lower temperatures in the response curve for the 94 Å band. Fe VIII 7f–3d transitions at 93.469 and 93.616 Å have been identified by Ramonas & Ryabtsev (1980). Approximate excitation data for these transitions were estimated by Czyzak & Krueger (1966), and a proper scattering calculation was needed. The presence of Fe IX 5f–3d transitions in the 94 Å region has been proposed by Lepson et al. (2002), but appropriate calculations have been missing.

In this work, we have therefore carried out calculations for Fe VIII and Fe IX using a new distorted wave (DW) development of the AUTOSTRUCTURE code, described in Badnell (2011) and outlined below. We have used this new code to obtain collisional and radiative data for levels up to $n = 6$ for Fe IX and $n = 7$ for Fe VIII. We have merged the data for the higher energy levels with those of the lower R-matrix ones ($n = 3$), previously available, to build an atomic model and calculate spectral line intensities, to compare with observations. Recently, Foster & Testa (2011) have also carried out atomic calculations for the Fe IX 5f−3d transitions using the Flexible Atomic Code (FAC, see Gu 2003). Towards the end of the paper, we briefly compare our results with theirs.

The discussion in this paper focuses on transitions from $n = 4$–7 configurations observed in the Soft X-rays, from 50 to 170 Å. These atomic data are needed, because there are a large number of lines (many of which are still unidentified) in this wavelength range. This spectral range is also routinely observed now by the SDO Extreme ultraviolet Variability Experiment (EVE). EVE includes two spectrographs and multiple photometers for measuring the solar EUV irradiance from 1 to 1220 Å (Woods et al. 2010). The EUV spectra are from two Multiple EUV Grating Spectrographs (MEGS) in the 50–380 Å and 350–1050 Å spectral ranges, with ≃1 Å spectral resolution.

The paper is organised as follows. In Sect. 2, we give details of the methods used for the atomic structure and electron scattering calculations. The Fe IX and Fe VIII calculations are discussed in Sects. 3 and 4, respectively. Comparisons are made with the results of previous publications. In Sect. 5 we benchmark the atomic data we have calculated for Fe VIII and Fe IX against solar and laboratory spectra. Our conclusions are given in Sect. 6.

⋆ A complete list of calculated energies, radiative data and thermally averaged collision strengths is only available at the CDS via anonymous ftp to cdsarc.u-strasbg.fr (130.79.128.5) or via http://cdsarc.u-strasbg.fr/viz-bin/qcat?J/A+A/537/A22

2. Method

The atomic structure calculations were carried out using the program AUTOSTRUCTURE (Badnell 1997) which constructs target wavefunctions using radial wavefunctions calculated in a scaled Thomas-Fermi-Dirac statistical model potential. The scaling parameters were determined by minimising the sum of the energies of all the target terms, computed in LS-coupling, i.e. neglecting all relativistic effects.

The Breit-Pauli distorted wave calculations were carried-out using the AUTOSTRUCTURE code. Full details of this recent development of the code are found in Badnell (2011). Although it bears some superficial similarities with the historic UCL-DW code (Eissner 1998) due to their common SUPERSTRUCTURE heritage (Eissner et al. 1974), it is an independent implementation which differs fundamentally from the UCL-DW code in a number of important ways. We note salient points of the implementation. It places no restrictions of the atomic structure. Two-body fine-structure can be included if desired, for example. The continuum distorted waves are calculated using the same form for the distorting potential as specified for the target, but now for the $(N + 1)$-electron problem. Non-relativistic or kappa-averaged relativistic orbitals can be used. Unlike the bound-free problem (e.g. autoionization) the continuum orbitals are not orthogonalized to the bound orbitals, nor are the "zero" overlaps neglected. Rather, the appropriate exchange overlap integrals are determined. The electrostatic and, optionally, two-body non-fine-structure $(N + 1)$-electron interaction Hamiltonian for the collision problem is determined in an unmixed LS-coupling representation. It is then transformed to an LSJ representation. The two-body fine-structure collisional interaction can be added, optionally, at this stage. The full $(N + 1)$-electron interaction Hamiltonian is transformed to a full Breit-Pauli jK-coupling representation (i.e. including both configuration and fine-structure target mixing) in the same manner as is done for the (inner-region) Breit-Pauli R-matrix.

Collision strengths are calculated at the same set of final scattered energies for all transitions. Zero gives all threshold transitions, for example. A small continuum interpolation basis is used to enable the interaction Hamiltonian to be evaluated at the appropriate initial scattering energy for each transition. "Top-up" in the contribution of high partial waves is done using the same Breit-Pauli methods and subroutines implemented in the R-matrix outer-region code STGF. The implementation is designed for efficiency in determining collision strengths from a low-lying set of (user specifiable) "metastable" levels to all possible "spectroscopic" excited states. "Correlation" levels/terms/configurations can be flagged for efficiency so that they contribute only to the target description. The final deliverable is a (type-5) *adf04* file (Summers 2006) which contains energy levels, radiative rates, ordinary collision strengths (as a function of final scattered energy) and infinite energy Born limits (and line strengths). These ordinary collision strengths can then be convoluted with any desired electron energy distribution. A utility code (`adf04_om2ups.f`) is provided which converts this file to the more familiar (type-3) *adf04* file which contains Maxwell-averaged effective collision strengths.

We note that resonances are omitted in the first instance. Since resonances in electron-impact excitation are just the complement of dielectronic recombination then their contribution can be determined independently, if desired. Alternatively, our approach lends itself to complementing the results of an R-matrix calculation, as herein, since resonances are more prominent in low-lying transitions. There is also compatibility in atomic structure which aids merging of the two datasets. Starting with the R-matrix target structure, which may be much larger than that for which collision data is calculated, additional orbitals and configurations included in the DW calculation should not perturb the original structure too much. If it does then the original R-matrix structure is questionable.

In addition to the original tests and comparisons (Badnell 2011) some further comparisons of collision strengths from the AUTOSTRUCTURE DW code have been made with both FAC and (background) R-matrix collision strengths, and which emphasise the importance of the atomic structure in such – see Liang & Badnell (2011) and Liang et al. (2011).

3. Fe IX

A significant number of transitions from $n = 4, 5$ levels for this ion remain unidentified. Kruger et al. (1937) identified the two strong decays from the 4s levels to the ground state. Alexander et al. (1965) later identified four decays from the 4d and 5s levels. Wagner & House (1971) were the first to identify 12 transitions from the $3p^5\ 3d$–$3p^5\ 4f$ array, in the 111.69–116.81 Å spectral range. We adopt the measurements from Fawcett et al. (1972) who revised the Wagner & House (1971) wavelengths. Young (2009) identified three lines from the $3s^2\ 3p^4\ 3d^2$ configuration and one from the $3s^2\ 3p^5\ 4p$ configuration. Young & Landi (2009) identified some more transitions from the $3s^2\ 3p^4\ 3d^2$ configuration. Landi & Young (2009) identified two more transitions from the $3s^2\ 3p^5\ 4p$ configuration.

Lines from Fe IX have been observed in the extreme ultraviolet with an electron beam ion trap (EBIT) by Beiersdorfer et al. (1999) and Lepson et al. (2002). Lepson et al. (2002) suggested that a few weak lines observed around 94 Å arise from 5f–3d transitions, however a firm identification was not provided.

Radiative data for this ion have been calculated by a number of authors. Aggarwal et al. (2006) calculated radiative data with the General purpose Relativistic Atomic Structure Package (GRASP) for transitions between some $n = 3$ and the $3s^2\ 3p^5\ 4l$ configurations.

Verma et al. (2006) produced a large-scale structure calculation using Hibbert's CIV3 Program and semi-empirical corrections to obtain a good match in level energies for those known. They included some $n = 3, 4, 5$ configurations, but not the $3s^2\ 3p^5\ 5f$. The configuration $3s^2\ 3p^3\ 3d^3$, which is important for configuration interaction, was omitted from their calculations.

FAC atomic structure calculations were carried out by Landi & Young (2009) up to $n = 4$.

In terms of electron excitation data, the most accurate calculation so far is from Storey et al. (2002). These data are included in CHIANTI v.6 (Dere et al. 2009). Storey et al. (2002) performed an R-matrix calculation, producing collisional excitations rates among the lowest 140 energy levels, in six configurations, which include levels from the $3s^2\ 3p^5\ 4s$ and $3s^2\ 3p^5\ 4p$ configurations. His target had 12 configurations, of which 6 were included as correlation configurations.

We have run several structure calculations with various configurations (12, 27, 45 and 67 configuration calculations). The 12 configuration target is identical to that of Storey et al. (2002). Our final choice for the scattering calculation is the largest run, where the target wavefunctions are expanded in the 67 configuration basis listed in Table 1. Those configurations listed above the horizontal line in Table 1 are spectroscopic configurations. Those below this line are present solely for correlation purposes. The Thomas-Fermi-Dirac scaling parameters are also given in Table 1.

Table 1. Electron configuration basis for the DW calculation and orbital scaling parameters for Fe IX.

Configurations		Scaling parameters			
even	odd				
$3s^2\ 3p^6$	$3s^2\ 3p^5\ 3d$	1s:	1.4171	2s:	1.1241
$3s\ 3p^6\ 3d$	$3s\ 3p^5\ 3d^2$	2p:	1.0672	3s:	1.1499
$3s^2\ 3p^4\ 3d^2$	$3s^2\ 3p^5\ 4s$	3p:	1.1294	3d:	1.1371
$3s^2\ 3p^5\ 4p$	$3s^2\ 3p^5\ 4d$	4s:	1.1524	4p:	1.1254
$3s\ 3p^6\ 4s$	$3s\ 3p^6\ 4p$	4d:	1.1308	4f:	1.2586
$3s\ 3p^6\ 4d$	$3s\ 3p^6\ 4f$	5s:	1.1667	5p:	1.1366
$3s^2\ 3p^5\ 4f$	$3s^2\ 3p^5\ 5s$	5d:	1.1650	5f:	1.7195
$3p^6\ 3d^2$	$3s^2\ 3p^5\ 5d$	5g:	1.6330	6s:	1.1935
$3s^2\ 3p^5\ 5p$	$3s^2\ 3p^5\ 5g$	6p:	1.1871	6d:	1.2061
$3s^2\ 3p^5\ 5f$	$3s^2\ 3p^5\ 6s$	6f:	1.7170	6g:	1.6577
$3s^2\ 3p^5\ 6p$	$3s^2\ 3p^5\ 6d$				
$3s^2\ 3p^5\ 6f$	$3s^2\ 3p^5\ 6g$				
- -					
$3s^2\ 3p^4\ 3d\ 4s$	$3s^2\ 3p^4\ 3d\ 4p$				
$3s^2\ 3p^4\ 3d\ 4d$	$3s^2\ 3p^4\ 3d\ 4f$				
$3s\ 3p^4\ 3d^3$	$3s^2\ 3p^3\ 3d^3$				
$3s\ 3p^6\ 5s$	$3p^5\ 3d^3$				
$3s\ 3p^6\ 5d$	$3s\ 3p^6\ 5p$				
$3s\ 3p^6\ 5g$	$3s\ 3p^6\ 5f$				
$3s^2\ 3p^4\ 3d\ 5s$	$3s^2\ 3p^4\ 3d\ 5p$				
$3s^2\ 3p^4\ 3d\ 5d$	$3s^2\ 3p^4\ 3d\ 5f$				
$3s^2\ 3p^4\ 3d\ 5g$	$3s\ 3p^5\ 3d\ 5s$				
$3s\ 3p^5\ 3d\ 5p$	$3s\ 3p^5\ 3d\ 5d$				
$3s\ 3p^5\ 3d\ 5f$	$3s\ 3p^5\ 3d\ 5g$				
$3s\ 3p^6\ 6s$	$3s\ 3p^6\ 6p$				
$3s\ 3p^6\ 6d$	$3s\ 3p^6\ 6f$				
$3s\ 3p^6\ 6g$	$3s^2\ 3p^4\ 3d\ 6p$				
$3s^2\ 3p^4\ 3d\ 6s$	$3s^2\ 3p^4\ 3d\ 6f$				
$3s^2\ 3p^4\ 3d\ 6d$	$3s\ 3p^5\ 3d\ 6s$				
$3s^2\ 3p^4\ 3d\ 6g$	$3s\ 3p^5\ 3d\ 6d$				
$3s\ 3p^5\ 3d\ 6p$	$3s\ 3p^5\ 3d\ 6g$				
$3s\ 3p^5\ 3d\ 6f$	$3s\ 3p^5\ 3d\ 4s$				
$3s^2\ 3p^2\ 3d^4$	$3s\ 3p^5\ 3d\ 4d$				
$3s^2\ 3p^4\ 4p^2$					
$3s\ 3p^5\ 3d\ 4p$					
$3s\ 3p^5\ 3d\ 4f$					

Notes. The configurations below the dashed line are correlation configurations.

Table 2. Level energies for Fe IX.

i	Conf.	Lev.	E_{exp}	E_{calc}
1	$3s^2\ 3p^6$	$^1S_0$	0.0	0.0
2	$3s^2\ 3p^5\ 3d$	$^3P_0$	405772.0	412902 (−7130)
3	$3s^2\ 3p^5\ 3d$	$^3P_1$	408315.1	415718 (−7403)
4	$3s^2\ 3p^5\ 3d$	$^3P_2$	413669.2	421482 (−7813)
5	$3s^2\ 3p^5\ 3d$	$^3F_4$	425809.8	435212 (−9402)
6	$3s^2\ 3p^5\ 3d$	$^3F_3$	429310.9	438647 (−9336)
7	$3s^2\ 3p^5\ 3d$	$^3F_2$	433818.8	443252 (−9433)
8	$3s^2\ 3p^5\ 3d$	$^3D_3$	455612.2	465650 (−10038)
9	$3s^2\ 3p^5\ 3d$	$^1D_2$	456752.7	467102 (−10349)
10	$3s^2\ 3p^5\ 3d$	$^3D_1$	460616.0	470561 (−9945)
11	$3s^2\ 3p^5\ 3d$	$^3D_2$	462616.6	473000 (−10383)
12	$3s^2\ 3p^5\ 3d$	$^1F_3$	465828.4	476321 (−10493)
13	$3s^2\ 3p^5\ 3d$	$^1P_1$	584546	601508 (−16962)
14	$3s\ 3p^6\ 3d$	$^3D_1$	726734	737860 (−11126)
15	$3s\ 3p^6\ 3d$	$^3D_2$	727560	738828 (−11268)
16	$3s\ 3p^6\ 3d$	$^3D_3$	728935	740423 (−11488)
17	$3s\ 3p^6\ 3d$	$^1D_2$	749871	761945 (−12074)
94	$3s^2\ 3p^4\ 3d^2$	$^3G_4$	955790	982417 (−26627)
95	$3s^2\ 3p^4\ 3d^2$	$^3G_5$	956322	982823 (−26501)
96	$3s^2\ 3p^4\ 3d^2$	$^3G_3$	956787	983911 (−27124)
97	$3s^2\ 3p^5\ 4s$	$^3P_1$	950498	989102 (−38604)
107	$3s^2\ 3p^5\ 4s$	$^1P_1$	965568	1004712 (−39144)
140	$3s^2\ 3p^5\ 4p$	$^1S_0$	1089949	1126230 (−36281)
196	$3s^2\ 3p^5\ 4d$	$^1P_1$	1198222	1240063 (−41841)
210	$3s^2\ 3p^5\ 4d$	$^3D_1$	1213150	1254981 (−41831)
237	$3s^2\ 3p^5\ 4f$	$^3D_1$	1300923	1344314 (−43391)
238	$3s^2\ 3p^5\ 4f$	$^3D_2$	1302841	1346283 (−43442)
239	$3s^2\ 3p^5\ 4f$	$^3G_5$	1304598	1348616 (−44018)
241	$3s^2\ 3p^5\ 4f$	$^3D_3$	1305762	1349426 (−43664)
243	$3s^2\ 3p^5\ 4f$	$^3G_4$	1306319	1350544 (−44225)
245	$3s^2\ 3p^5\ 4f$	$^3G_3$	1310158	1354494 (−44336)
246	$3s^2\ 3p^5\ 4f$	$^1G_4$	1311755	1356693 (−44938)
247	$3s^2\ 3p^5\ 4f$	$^3F_2$	1316758	1362088 (−45330)
250	$3s^2\ 3p^5\ 4f$	$^1F_3$	1323657	1368060 (−44403)
253	$3s^2\ 3p^5\ 4f$	$^3F_3$	1324715	1369302 (−44587)
254	$3s^2\ 3p^5\ 4f$	$^3F_4$	1324876	1369536 (−44660)
256	$3s^2\ 3p^5\ 4f$	$^1D_2$	1331244	1376065 (−44821)
261	$3s\ 3p^6\ 4p$	$^1P_1$	1371910	1397410 (−25500)
263	$3s^2\ 3p^5\ 5s$	$^1P_1$	1358363	1401819 (−43456)
265	$3s^2\ 3p^5\ 5s$	$^3P_1$	1372683	1415509 (−42826)
302	$3s^2\ 3p^5\ 5f$	$^3G_5$	1513000	1567244 (−54244)
305	$3s^2\ 3p^5\ 5f$	$^3G_4$	1516500	1568654 (−52154)
308	$3s^2\ 3p^5\ 5f$	$^1F_3$	1519790	1570945 (−51154)
311	$3s^2\ 3p^5\ 5f$	$^3F_4$	1518650	1572181 (−53531)
316	$3s^2\ 3p^5\ 5f$	$^3F_2$	1523654	1575726 (−52072)
318	$3s^2\ 3p^5\ 5f$	$^3F_3$	1531107	1584992 (−53885)
319	$3s^2\ 3p^5\ 5f$	$^1G_4$	1534318	1585696 (−51377)

Notes. The columns provide: our experimental level energies E_{exp} (cm^{-1}), those for the 67 configuration target (Table 1) E_{calc} (cm^{-1}). Values in parentheses indicate differences between the observed and theoretical energies. The full dataset is available at the CDS.

In Table 2 we list the calculated and, where available, experimental energies for a sample of levels of the target. A complete list of the calculated energies of all 379 levels of the target is available at the CDS.

Table 3 contains a comparison of transition probabilities for a sample of the stronger transitions. Transition probabilities are provided for our 27, 45 and 67 configuration targets as well as those calculated by Storey et al. (2002) (in agreement with our 12 configuration calculation), Landi (2011, priv. comm.) corresponding to those of Landi & Young (2009) and Verma et al. (2006). Overall agreement (to within a relative 20%) is found, with the exception of the $3p^6\ ^1S_0$–$3p^5\ 5s\ ^1P_1$ and $3p^6\ ^1S_0$–$3p^5\ 5s\ ^3P_1$ transitions for which there are substantial differences. As Verma et al. pointed out, the $3s^2\ 3p^5\ 5s\ ^1P_1$ and $^3P_1$ are highly mixed, and these levels also mix with the $3s\ 3p^6\ 4p\ ^1P_1$ level. In our largest structure run, 67 configurations, level 263 ($5s\ ^1P_1$) is composed of 38% ($5s\ ^1P_1$), 32% ($5s\ ^3P_1$) and 10% ($3s\ 3p^6\ 4p\ ^1P_1$), while level 265 ($5s\ ^3P_1$) is composed of 55% ($5s\ ^3P_1$), and 41% ($5s\ ^1P_1$). Our predicted energy difference between the two 5s levels (13690 cm^{-1}) is close to the observed one (14 530 cm^{-1}). For our smaller structure calculations the mixing is: for 27 configurations, $3s^2\ 3p^5\ 5s\ ^1P_1$ is 52% ($5s\ ^1P_1$) plus 45% ($5s\ ^3P_1$); for 45 configurations, $3s^2\ 3p^5\ 5s\ ^1P_1$ is 55% ($5s\ ^1P_1$) plus 44% ($5s\ ^3P_1$). This change is mainly due to the position of the $3s\ 3p^6\ 4p\ ^1P_1$ level. Verma et al. quote mixing values for $3s^2\ 3p^5\ 5s\ ^1P_1$ as 55% ($5s\ ^1P_1$) plus 31% ($5s\ ^3P_1$), but they also mention that the $3s\ 3p^6\ 4p\ ^1P_1$ level is coupled with the $3s^2\ 3p^5\ 5s\ ^3P_1$ level, and that they have carried out some semi-empirical adjustments to the Hamiltonian. Our ab-initio model predicts the

Table 3. Transition probabilities for Fe IX.

Levels	$A_{ji}(s^{-1})$					
	27 Conf.	45 Conf.	67 Conf.	Storey 02	Verma 06	Landi 09
$3s^2\ 3p^6\ {}^1S_0$–$3s^2\ 3p^5\ 4s\ {}^1P_1$	5.40×10^{10}	5.02×10^{10}	5.06×10^{10}	4.1×10^{10}	4.12×10^{10}	4.64×10^{10}
$3s^2\ 3p^6\ {}^1S_0$–$3s^2\ 3p^5\ 4s\ {}^3P_1$	2.08×10^{10}	2.35×10^{10}	2.43×10^{10}	1.9×10^{10}	2.34×10^{10}	2.20×10^{10}
$3s^2\ 3p^6\ {}^1S_0$–$3s^2\ 3p^5\ 5s\ {}^1P_1$	1.69×10^{10}	2.66×10^{10}	4.24×10^{10}		8.98×10^{9}	
$3s^2\ 3p^6\ {}^1S_0$–$3s^2\ 3p^5\ 5s\ {}^3P_1$	1.40×10^{10}	1.50×10^{10}	1.85×10^{10}		3.98×10^{10}	
$3s^2\ 3p^6\ {}^1S_0$–$3s^2\ 3p^5\ 6s\ {}^1P_1$	8.80×10^{9}	1.14×10^{10}	1.06×10^{10}			
$3s^2\ 3p^6\ {}^1S_0$–$3s^2\ 3p^5\ 6s\ {}^3P_1$	4.71×10^{9}	6.30×10^{9}	4.79×10^{9}			

decay from the 5s $^1P_1$ level to be about twice as strong the decay from the 5s $^3P_1$. Both Alexander et al. (1965) and Lepson et al. (2002) indicate a ratio of two between these two lines, in agreement with our prediction. We cannot understand why the transition probability given by Verma et al. (their Table 5, our Table 3) for the transition 5s $^1P_1$ to the ground level is signifcantly less than that for 5s $^3P_1$ to the ground level. This seems most unusual, even if the mixing with the 3s $3p^6$ 4p $^1P_1$ level is more significant than we have calculated.

For our largest structure calculation, 67 configurations, the level $3s^2\ 3p^5\ 4s\ {}^1P_1$ is composed of 66% (4s $^1P_1$) plus 30% (4s $^3P_1$). These values are close to those of Verma, 61% (4s $^1P_1$) plus 36% (4s $^3P_1$). Our transition probabilities for 4s transitions to the ground (Table 3) are in reasonable agreement with Verma et al., in contrast to those for 5s to the ground.

An R-matrix calculation including all of the excited levels for $n = 5$ & 6 would be quite demanding. We have instead used the distorted wave AUTOSTRUCTURE code to calculate collision strengths for the high lying levels of Fe IX. These calculations do not include low-energy resonance effects, which could be significant for some transitions. As a result we use the collision strengths from the R-matrix calculation of Storey et al. (2002) for lower levels where available.

Levels up to level 79 contain some metastable levels. For the 79 energetically lowest levels collision strengths are calculated between themselves and up to all excited states. Collisional transitions between excited states higher than level 79 are omitted. Radiative data is calculated for all transitions.

Table 4 contains predicted intensities for the strongest Fe IX lines in the 50–170 Å range. The relative intensities (photons) $Int = N_j A_{ji}/N_e$ are normalised to the strongest transition and were calculated at electron densities of 10^8 and 10^{12} cm^{-3} and log T[K] = 5.85, typical of the quiet solar corona, and of high-density laboratory plasmas. Weighted oscillator strengths gf and A-values (s^{-1}) are shown. Also included are the calculated and, where available, experimental wavelengths for these lines. The strongest lines are the decays from the $3s^2\ 3p^5$ 4s,d to the ground state, and the 3d–4f transitions.

One issue of concern is the reliability of DW results for transitions to the $n = 4, 5$ levels. A comparison between the R-matrix and DW results for the 3p–4s transitions shows that resonances attached to higher-lying levels are significant. This is caused by the the fact that the $3s^2\ 3p^5$ 4s levels are relatively low-lying, and the background collision strength is small, hence the contribution from resonances can have an important effect.

For example, the collision strength for the $3s^2\ 3p^6\ {}^1S_0$–$3s^2\ 3p^5\ 4s\ {}^1P_1$ transition is shown in Fig. 1 (top). Good agreement in the background values is found with the R-matrix results from Storey et al. (2002), however the large contributions from the resonances near threshold do affect the thermally-averaged collision strength (shown in Fig. 1, below), with a significant increase

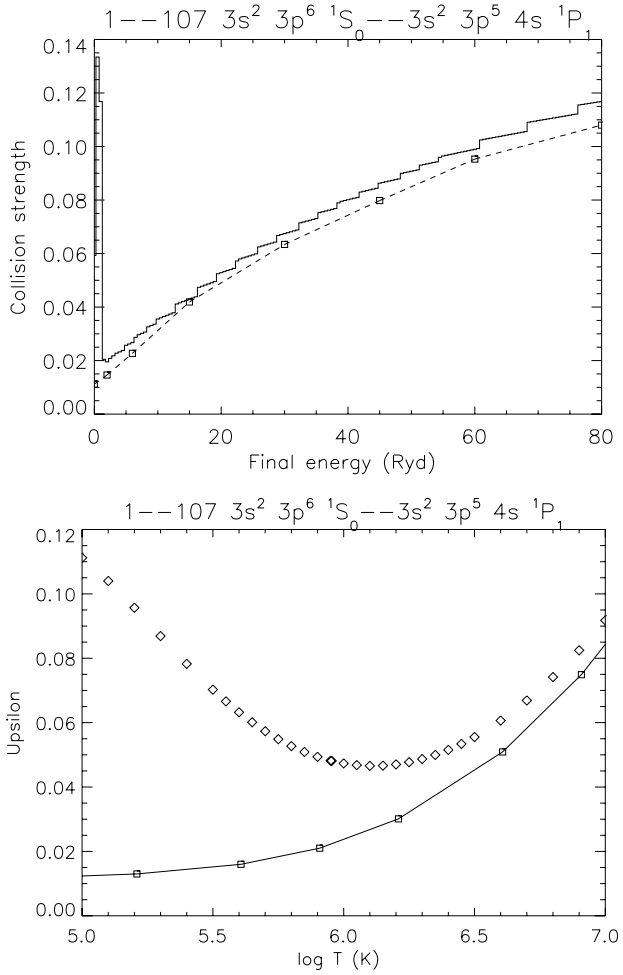

Fig. 1. *Top*: collision strength for the $3s^2\ 3p^6\ {}^1S_0$–$3s^2\ 3p^5\ 4s\ {}^1P_1$ transition of Fe IX. Squares with dashed line from present results. Histogram from Storey et al. (2002). *Bottom*: thermally averaged collision strength for the $3s^2\ 3p^6\ {}^1S_0$–$3s^2\ 3p^5\ 4s\ {}^1P_1$ transition. Solid line with squares from present results. Diamonds from Storey et al. (2002).

(by a factor of two near peak Fe IX abundance in equilibrium). Further investigation indicates that the main contribution comes from the $3s^2\ 3p^5\ 4p\ {}^1S_0$ level.

Figure 2 shows the collision strength for the strong $3s^2\ 3p^6\ {}^1S_0$–$3s^2\ 3p^5\ 4p\ {}^1S_0$ transition. Again, good agreement in the background values is found, as expected. The R-matrix result does not contain resonances because the $3s^2\ 3p^5\ 4p\ {}^1S_0$ level was the highest one included in the Storey et al. (2002) calculation. It is interesting to note the large collision strength for this forbidden transition between configurations with the same parity. This was a somewhat unexpected result. The $3s^2\ 3p^5\ 4p\ {}^1S_0$

Table 4. List of the strongest Fe IX lines in the 50–130 Å range.

i–j	Levels	*Int* 10^8	*Int* 10^{12}	gf	$A_{ji}(s^{-1})$	λ_{exp}(Å)	λ_{th}(Å)
1–107	$3s^2\ 3p^6\ ^1S_0$–$3p^5\ 4s\ ^1P_1$	1.0	0.76	0.18	4.1×10^{10}	103.566	98.08 (−5.5)
5–239	$3p^5\ 3d\ ^3F_4$–$3p^5\ 4f\ ^3G_5$	0.53	0.45	5.35	2.7×10^{11}	113.793	108.37 (−5.4)
1–97	$3s^2\ 3p^6\ ^1S_0$–$3p^5\ 4s\ ^3P_1$	0.52	0.44	8.3×10^{-2}	1.9×10^{10}	105.208	99.60 (−5.6)
13–256	$3p^5\ 3d\ ^1P_1$–$3p^5\ 4f\ ^1D_2$	0.22	0.14	1.87	1.5×10^{11}	133.923	126.34 (−7.6)
6–243	$3p^5\ 3d\ ^3F_3$–$3p^5\ 4f\ ^3G_4$	0.22	0.27	3.55	2.2×10^{11}	114.024	108.55 (−5.5)
1–196	$3s^2\ 3p^6\ ^1S_0$–$3p^5\ 4d\ ^1P_1$	0.20	0.13	0.36	1.2×10^{11}	83.457	80.64 (−2.8)
1–210	$3s^2\ 3p^6\ ^1S_0$–$3p^5\ 4d\ ^3D_1$	0.15	9.9×10^{-2}	0.12	4.3×10^{10}	82.430	79.68 (−2.7)
5–302	$3p^5\ 3d\ ^3F_4$–$3p^5\ 5f\ ^3G_5$	0.14	0.12	2.07	1.6×10^{11}	91.980	87.61 (−4.4)
10–247	$3p^5\ 3d\ ^3D_1$–$3p^5\ 4f\ ^3F_2$	0.12	8.6×10^{-2}	1.29	1.4×10^{11}	116.803	110.93 (−5.9)
4–241	$3p^5\ 3d\ ^3P_2$–$3p^5\ 4f\ ^3D_3$	9.1×10^{-2}	0.21	2.45	2.0×10^{11}	112.096	106.87 (−5.2)
10–256	$3p^5\ 3d\ ^3D_1$–$3p^5\ 4f\ ^1D_2$	8.9×10^{-2}	5.6×10^{-2}	0.55	6.0×10^{10}	114.860	109.24 (−5.6)
8–246	$3p^5\ 3d\ ^3D_3$–$3p^5\ 4f\ ^1G_4$	7.9×10^{-2}	0.25	3.47	2.0×10^{11}	116.803	110.98 (−5.8)
7–245	$3p^5\ 3d\ ^3F_2$–$3p^5\ 4f\ ^3G_3$	7.9×10^{-2}	0.16	2.37	1.9×10^{11}	114.111	108.62 (−5.5)
5–366	$3p^5\ 3d\ ^3F_4$–$3p^5\ 6f\ ^3G_5$	7.7×10^{-2}	6.7×10^{-2}	1.64	1.6×10^{11}	–	79.12
3–238	$3p^5\ 3d\ ^3P_1$–$3p^5\ 4f\ ^3D_2$	5.7×10^{-2}	7.4×10^{-2}	1.40	1.6×10^{11}	111.791	106.61 (−5.2)
13–247	$3p^5\ 3d\ ^1P_1$–$3p^5\ 4f\ ^3F_2$	5.7×10^{-2}	4.1×10^{-2}	0.84	6.5×10^{10}	136.572	128.61 (−8.0)
13–276	$3p^5\ 3d\ ^1P_1$–$3p^5\ 5p\ ^1S_0$	5.6×10^{-2}	3.2×10^{-2}	6.5×10^{-3}	3.2×10^{9}	–	113.08
10–271	$3p^5\ 3d\ ^3D_1$–$3p^5\ 5p\ ^3P_0$	5.4×10^{-2}	3.1×10^{-2}	4.9×10^{-2}	3.1×10^{10}	–	100.76
6–305	$3p^5\ 3d\ ^3F_3$–$3p^5\ 5f\ ^3G_4$	5.2×10^{-2}	6.1×10^{-2}	1.33	1.3×10^{11}	91.980	87.77 (−4.2)
12–254	$3p^5\ 3d\ ^1F_3$–$3p^5\ 4f\ ^3F_4$	5.0×10^{-2}	0.24	3.52	2.1×10^{11}	116.408	110.66 (−5.8)
13–326	$3p^5\ 3d\ ^1P_1$–$3p^5\ 5f\ ^1D_2$	4.9×10^{-2}	3.3×10^{-2}	0.73	9.5×10^{10}	–	99.51
13–379	$3p^5\ 3d\ ^1P_1$–$3p^5\ 6f\ ^1D_2$	4.6×10^{-2}	3.0×10^{-2}	0.50	8.4×10^{10}	–	88.30
10–276	$3p^5\ 3d\ ^3D_1$–$3p^5\ 5p\ ^1S_0$	4.6×10^{-2}	2.6×10^{-2}	4.0×10^{-3}	2.7×10^{9}	–	99.18
10–316	$3p^5\ 3d\ ^3D_1$–$3p^5\ 5f\ ^3F_2$	3.5×10^{-2}	2.4×10^{-2}	0.44	7.2×10^{10}	94.070	89.68 (−4.4)
11–253	$3p^5\ 3d\ ^3D_2$–$3p^5\ 4f\ ^3F_3$	3.4×10^{-2}	0.16	2.76	2.1×10^{11}	115.996	110.29 (−5.7)
2–237	$3p^5\ 3d\ ^3P_0$–$3p^5\ 4f\ ^3D_1$	3.3×10^{-2}	3.5×10^{-2}	0.66	1.3×10^{11}	111.713	106.55 (−5.2)
9–250	$3p^5\ 3d\ ^1D_2$–$3p^5\ 4f\ ^1F_3$	3.2×10^{-2}	0.15	2.42	1.9×10^{11}	115.353	109.73 (−5.6)
17–349	$3p^6\ 3d\ ^1D_2$–$3p^6\ 4f\ ^1F_3$	2.8×10^{-2}	1.9×10^{-2}	2.34	1.7×10^{11}	–	111.34
3–237	$3p^5\ 3d\ ^3P_1$–$3p^5\ 4f\ ^3D_1$	2.7×10^{-2}	2.9×10^{-2}	0.55	1.1×10^{11}	112.031	106.84 (−5.2)
6–368	$3p^5\ 3d\ ^3F_3$–$3p^5\ 6f\ ^3G_4$	2.6×10^{-2}	3.1×10^{-2}	0.87	1.0×10^{11}	–	79.23
8–311	$3p^5\ 3d\ ^3D_3$–$3p^5\ 5f\ ^3F_4$	2.6×10^{-2}	6.9×10^{-2}	1.44	1.3×10^{11}	94.070	89.56 (−4.5)
13–316	$3p^5\ 3d\ ^1P_1$–$3p^5\ 5f\ ^3F_2$	2.5×10^{-2}	1.7×10^{-2}	0.41	5.2×10^{10}	–	100.89
1–280	$3s^2\ 3p^6\ ^1S_0$–$3p^5\ 5d\ ^1P_1$	2.5×10^{-2}	1.6×10^{-2}	0.16	7.8×10^{10}	–	66.39
11–256	$3p^5\ 3d\ ^3D_2$–$3p^5\ 4f\ ^1D_2$	2.5×10^{-2}	1.6×10^{-2}	0.16	1.7×10^{10}	115.124	109.48 (−5.6)
4–304	$3p^5\ 3d\ ^3P_2$–$3p^5\ 5f\ ^3D_3$	2.4×10^{-2}	4.3×10^{-2}	0.81	1.0×10^{11}	–	86.59
4–238	$3p^5\ 3d\ ^3P_2$–$3p^5\ 4f\ ^3D_2$	2.4×10^{-2}	3.1×10^{-2}	0.59	6.7×10^{10}	112.464	107.23 (−5.2)
7–247	$3p^5\ 3d\ ^3F_2$–$3p^5\ 4f\ ^3F_2$	2.3×10^{-2}	1.7×10^{-2}	0.24	2.6×10^{10}	113.258	107.73 (−5.5)
10–326	$3p^5\ 3d\ ^3D_1$–$3p^5\ 5f\ ^1D_2$	2.2×10^{-2}	1.5×10^{-2}	0.26	4.3×10^{10}	–	88.58
8–241	$3p^5\ 3d\ ^3D_3$–$3p^5\ 4f\ ^3D_3$	2.1×10^{-2}	4.9×10^{-2}	0.63	4.7×10^{10}	117.626	111.88 (−5.7)
8–370	$3p^5\ 3d\ ^3D_3$–$3p^5\ 6f\ ^3F_4$	2.0×10^{-2}	4.5×10^{-2}	1.32	1.5×10^{11}	–	80.61
12–243	$3p^5\ 3d\ ^1F_3$–$3p^5\ 4f\ ^3G_4$	2.0×10^{-2}	2.4×10^{-2}	0.34	2.0×10^{10}	118.978	113.03 (−5.9)
1–263	$3s^2\ 3p^6\ ^1S_0$–$3p^5\ 5s\ ^1P_1$	1.9×10^{-2}	1.2×10^{-2}	9.7×10^{-2}	4.2×10^{10}	73.618	71.34 (−2.3)
13–339	$3p^5\ 3d\ ^1P_1$–$3p^5\ 6p\ ^1S_0$	1.9×10^{-2}	1.1×10^{-2}	4.6×10^{-3}	3.3×10^{9}	–	95.48
3–301	$3p^5\ 3d\ ^3P_1$–$3p^5\ 5f\ ^3D_2$	1.9×10^{-2}	2.0×10^{-2}	0.50	8.9×10^{10}	–	86.34
5–243	$3p^5\ 3d\ ^3F_4$–$3p^5\ 4f\ ^3G_4$	1.9×10^{-2}	2.3×10^{-2}	0.30	1.9×10^{10}	113.571	108.14 (−5.4)
12–319	$3p^5\ 3d\ ^1F_3$–$3p^5\ 5f\ ^1G_4$	1.8×10^{-2}	5.8×10^{-2}	1.40	1.3×10^{11}	93.590	89.30 (−4.3)
7–308	$3p^5\ 3d\ ^3F_2$–$3p^5\ 5f\ ^1F_3$	1.7×10^{-2}	3.0×10^{-2}	0.73	8.9×10^{10}	91.980	87.94 (−4.1)
11–318	$3p^5\ 3d\ ^3D_2$–$3p^5\ 5f\ ^3F_3$	1.6×10^{-2}	4.3×10^{-2}	0.96	1.1×10^{11}	93.590	89.10 (−4.5)
1–265	$3s^2\ 3p^6\ ^1S_0$–$3p^5\ 5s\ ^3P_1$	1.1×10^{-2}	7.3×10^{-3}	4.2×10^{-2}	1.8×10^{10}	72.850	70.65 (−2.2)
9–308	$3p^5\ 3d\ ^1D_2$–$3p^5\ 5f\ ^1F_3$	7.1×10^{-3}	1.3×10^{-2}	0.32	3.7×10^{10}	94.070	89.75 (−4.3)

Notes. The relative intensities (photons) $Int = N_j A_{ji}/N_e$ are normalised to the strongest transition and were calculated at electron densities of 10^8 and 10^{12} cm^{-3} and log T[K] = 5.85. Weighted oscillator strengths gf and A-values (s^{-1}) are shown. Experimental λ_{exp} (Å) and theoretical λ_{th} (Å) wavelengths are included. Values in parentheses indicate differences between the observed and theoretical wavelengths.

level decays via a strong dipole-allowed transition to the $3s^2\ 3p^5\ 3d\ ^1P_1$. An estimate of the wavelength for this transition with our 67 configuration calculation provides a value very close to that suggested by Young (2009), who identified this transition with a line in the Hinode EIS spectrum, at 197.862 Å. The observed intensity of this line, relative to that of other Fe IX transitions, is in good agreement with that predicted using the Storey et al. (2002) calculation, hence indirectly confirming the large collision strength from the ground state to the $3s^2\ 3p^5\ 4p\ ^1S_0$ level.

We have run various checks by looking at the collision strengths near thresholds for all transitions to levels with $n \geq 4$, and we believe that significant enhancements due to resonances

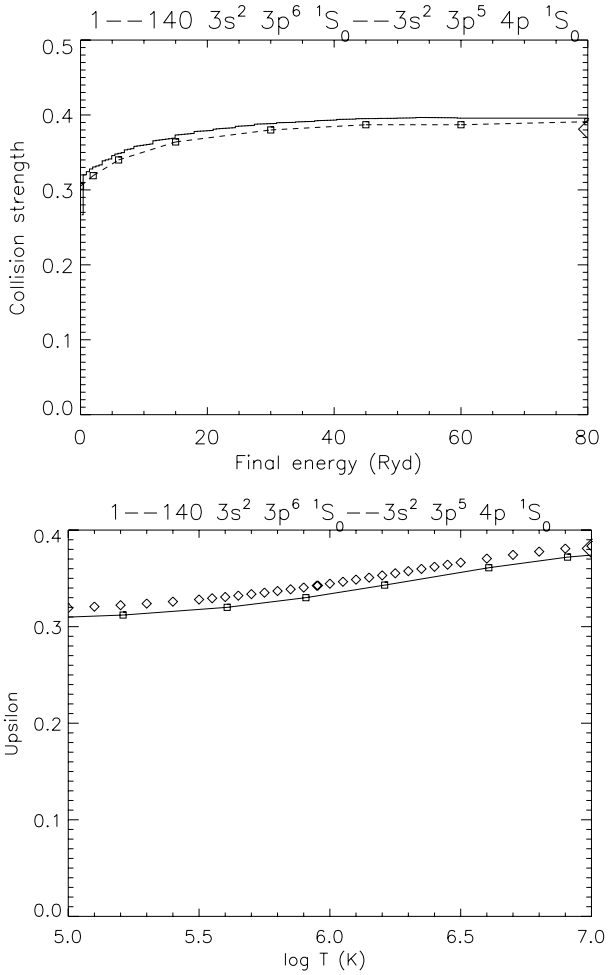

Fig. 2. *Top*: collision strength for the $3s^2\ 3p^6\ {}^1S_0$–$3s^2\ 3p^5\ 4p\ {}^1S_0$ transition of Fe IX. Squares with dashed line from present results. Histogram from Storey et al. (2002). *Bottom*: thermally averaged collision strength for the $3s^2\ 3p^6\ {}^1S_0$–$3s^2\ 3p^5\ 4p\ {}^1S_0$ transition. Solid line with squares from present results. Diamonds from Storey et al. (2002).

such as those occurring to the $3s^2\ 3p^5\ 4s$ levels should not be present. However, a further in-depth analysis, which is beyond the scope of this paper, is in progress.

4. Fe VIII

The identification of Fe VIII lines is reviewed in Del Zanna (2009). It started with Kruger & Weissberg (1937), who identified the main decays of the 4f, 5f, 6f and 7f levels. That study was followed by the fundamental laboratory work of Fawcett and co-workers on the *ZETA* spectrum (see Gabriel & Fawcett 1965), where a number of identifications for the EUV lines were provided. The main source of accurate wavelengths and further identifications came from the excellent work of Ramonas & Ryabtsev (1980).

Several atomic structure calculations exist in the literature. The latest ones are from Zeng et al. (2003), and Del Zanna (2009). Zeng et al. (2003) performed large-scale multi-configuration Hartree-Fock (MCHF) calculations for Fe VIII, to show the importance of including core-valence electron correlations. Del Zanna (2009) used AUTOSTRUCTURE and searched a "benchmark" configuration basis which reproduced well the positioning of a few key low $n = 3, 4$ mixed levels.

Table 5. Electron configuration basis for the DW calculation and orbital scaling parameters for Fe VIII.

Configurations		Scaling parameters	
even	odd		
$3s^2\ 3p^6\ 3d$	$3s^2\ 3p^5\ 3d^2$	1s: 1.4209	2s: 1.1289
$3s^2\ 3p^6\ 4s$	$3s^2\ 3p^6\ 4p$	2p: 1.0689	3s: 1.1503
$3s^2\ 3p^6\ 4d$	$3s^2\ 3p^6\ 4f$	3p: 1.1315	3d: 1.1576
$3s^2\ 3p^6\ 5s$	$3s^2\ 3p^6\ 5p$	4s: 1.1520	4p: 1.1194
$3s^2\ 3p^6\ 5d$	$3s^2\ 3p^6\ 5f$	4d: 1.1183	4f: 1.2042
$3s^2\ 3p^6\ 5g$	$3s^2\ 3p^6\ 6p$	5s: 1.1468	5p: 1.1229
$3s^2\ 3p^6\ 6s$	$3s^2\ 3p^6\ 6f$	5d: 1.1224	5f: 1.2009
$3s^2\ 3p^6\ 6d$	$3s^2\ 3p^6\ 6h$	5g: 1.2170	6s: 1.1489
$3s^2\ 3p^6\ 6g$	$3s^2\ 3p^6\ 7p$	6p: 1.1257	6d: 1.1250
$3s^2\ 3p^6\ 7s$	$3s^2\ 3p^6\ 7f$	6f: 1.2004	6g: 1.2184
$3s^2\ 3p^6\ 7d$	$3s^2\ 3p^5\ 3d\ 4s$	6h: 1.2174	7s: 1.1518
$3s^2\ 3p^4\ 3d^2\ 4f$		7p: 1.1291 7f: 1.2020	7d: 1.1275

Notes. The configuration below the dashed line is included for correlation purposes.

The additional $n > 4$ configurations were added to obtain a good target for these levels.

The latest electron scattering calculation for this ion is the R-matrix calculation by Griffin et al. (2000). It included the 33 terms and the 77 levels of the configurations $3s^2\ 3p^6\ 3d$, $3s^2\ 3p^5\ 3d^2$, $3s^2\ 3p^5\ 3d\ 4s$, $3s^2\ 3p^6\ 4s$, $3s^2\ 3p^6\ 4p$, $3s^2\ 3p^6\ 4d$ and $3s^2\ 3p^6\ 4f$ in the close-coupling expansion. The Griffin et al. (2000) data have been benchmarked by Del Zanna (2009) using Hinode EUV Imaging Spectrometer (EIS, see Culhane et al. 2007) observations, measurements found in the literature, and laboratory plates from B.C. Fawcett (see Del Zanna et al. 2004, for details on the benchmark method). The benchmark work showed that significant discrepancies (60% or so) between Hinode EIS observed intensities and those predicted with the Griffin et al. (2000) data exist for some lines. It was shown with the run of a large-scale AUTOSTRUCTURE "benchmark" calculation that this was due to missing configuration interaction (CI). The effects are subtle for some strong transitions arising from very mixed levels, and were also noted by Griffin et al. (2000).

In order to improve the Griffin et al. (2000) data, the collision strengths of the dipole-allowed transitions were scaled by Del Zanna (2009) according to the ratio of the gf values (and energies) in the Griffin et al. (2000) and the "benchmark" calculation. These data are included in CHIANTI v.7 and are adopted here.

The structure calculation by Del Zanna et al. (2004) was optimised for transitions between the $n = 3$ configurations. We have extended the structure (and scattering) calculations to levels up to $n = 7$.

An R-matrix calculation including all of the excited levels for $n = 5$, 6 & 7 would be quite demanding. Instead we use the distorted wave AUTOSTRUCTURE code to calculate collision strengths between levels of Fe VIII included in our structure calculations. Levels up to level 40 contain some metastable levels. For the 40 energetically lowest levels collision strengths are calculated between themselves and to all excited states. Collisional transitions between excited states higher than level 40 are omitted. Radiative data is calculated for all transitions.

The target wavefunctions are expanded in the 23 configuration basis listed in Table 5. The configuration $3s^2\ 3p^4\ 3d^2\ 4f$ is

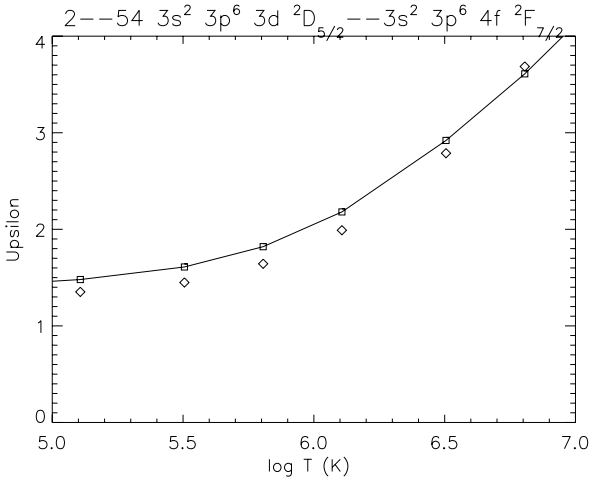

Fig. 3. Thermally averaged collision strength for the $3s^2\ 3p^6\ 3d\ ^2D_{5/2}$–$3s^2\ 3p^6\ 4f\ ^2F_{7/2}$ transition of Fe VIII. Solid line from present results. Diamonds from the R-matrix calculation of Griffin et al. (2000), adjusted by Del Zanna (2009).

present solely for correlation purposes. The resulting scaling parameters are also given in Table 5.

In Table 6 we list the calculated and, where available, experimental energies for a sample of levels of the target. A complete list of the calculated energies of all 104 levels of the target is available at the CDS.

Table 7 contains predicted intensities for the strongest Fe VIII lines in the 50–170 Å range. The relative intensities (photons) $Int = N_j A_{ji}/N_e$ are normalised to the strongest transition and were calculated at electron densities of 10^8 and 10^{12} cm^{-3} and $\log T[\mathrm{K}] = 5.6$. Weighted oscillator strengths gf and A-values (s^{-1}) are shown. Aslo included are the calculated and, where available, experimental wavelengths for these lines.

Thermally averaged collision strength for the $3s^2\ 3p^6\ 3d\ ^2D_{5/2}$–$3s^2\ 3p^6\ 4f\ ^2F_{7/2}$ transition of Fe VIII is plotted as a function of temperature in Fig. 3. The corresponding thermally averaged collision strength from the R-matrix calculation of Griffin et al. (2000), adjusted by Del Zanna, is found to be in very good agreement.

5. Benchmarking the atomic data

There is relatively little experimental data that we can use to benchmark the atomic data we have calculated. Most solar spectra have a relatively low resolution or are not calibrated. In terms of spectral resolution, the best soft X-ray solar spectrum is from Behring et al. (1972). They published a line list based on a LASP rocket flight that observed the entire Sun in the 60–385 Å region with very high-resolution (0.06 Å). A list of those lines observed in quiet conditions are included in Table 8. In terms of both spectral resolution and flux calibration, the best soft X-ray spectra of the quiet Sun are from Manson (1972). Manson (1972) provided an excellent list of lines observed in quiet and active conditions. The list of lines observed in quiet conditions are included in Table 8.

In terms of laboratory spectra, we use here the flux-calibrated theta-pinch spectra of Datla et al. (1975), and the EBIT measurements of Lepson et al. (2002). Lepson et al. provided some estimates of the line intensities. We are not sure about the actual flux calibration, so only lines not too far in wavelength are considered here.

Table 6. Level energies for Fe VIII.

i	Conf.	Lev.	E_{exp}	E_{calc}
1	$3s^2\ 3p^6\ 3d$	$^2D_{3/2}$	0.0	0.0
2	$3s^2\ 3p^6\ 3d$	$^2D_{5/2}$	1836	2038 (−202)
3	$3s^2\ 3p^5\ 3d^2$	$^4D_{1/2}$	391108	384967 (6141)
4	$3s^2\ 3p^5\ 3d^2$	$^4D_{3/2}$	391988	385994 (5994)
5	$3s^2\ 3p^5\ 3d^2$	$^4D_{5/2}$	393455	387729 (5726)
6	$3s^2\ 3p^5\ 3d^2$	$^4D_{7/2}$	395605	390297 (5308)
7	$3s^2\ 3p^5\ 3d^2$	$^4G_{11/2}$	–	408204
8	$3s^2\ 3p^5\ 3d^2$	$^4G_{9/2}$	–	409793
9	$3s^2\ 3p^5\ 3d^2$	$^4G_{7/2}$	–	411883
10	$3s^2\ 3p^5\ 3d^2$	$^4P_{5/2}$	–	413481
11	$3s^2\ 3p^5\ 3d^2$	$^4G_{5/2}$	–	414197
12	$3s^2\ 3p^5\ 3d^2$	$^4P_{3/2}$	–	416763
13	$3s^2\ 3p^5\ 3d^2$	$^4P_{1/2}$	–	419214
14	$3s^2\ 3p^5\ 3d^2$	$^4F_{3/2}$	–	423625
15	$3s^2\ 3p^6\ 4s$	$^2S_{1/2}$	–	424077
41	$3s^2\ 3p^6\ 4p$	$^2P_{1/2}$	510277	509420 (857)
42	$3s^2\ 3p^6\ 4p$	$^2P_{3/2}$	515550	512194 (3356)
43	$3s^2\ 3p^5\ 3d^2$	$^2P_{3/2}$	508518	521315 (−12797)
44	$3s^2\ 3p^5\ 3d^2$	$^2P_{1/2}$	520822	531502 (−10680)
45	$3s^2\ 3p^5\ 3d^2$	$^2F_{5/2}$	535910	553736 (−17826)
46	$3s^2\ 3p^5\ 3d^2$	$^2F_{7/2}$	541755	559876 (−18121)
47	$3s^2\ 3p^5\ 3d^2$	$^2P_{1/2}$	591964	611822 (−19858)
48	$3s^2\ 3p^5\ 3d^2$	$^2P_{3/2}$	595152	614976 (−19824)
49	$3s^2\ 3p^5\ 3d^2$	$^2D_{5/2}$	596465	624968 (−28503)
50	$3s^2\ 3p^5\ 3d^2$	$^2D_{3/2}$	597065	625143 (−28078)
51	$3s^2\ 3p^6\ 4d$	$^2D_{3/2}$	653717	657978 (−4261)
52	$3s^2\ 3p^6\ 4d$	$^2D_{5/2}$	654197	658461 (−4264)
53	$3s^2\ 3p^6\ 4f$	$^2F_{5/2}$	763703	728932 (34771)
54	$3s^2\ 3p^6\ 4f$	$^2F_{7/2}$	763799	729150 (34649)
61	$3s^2\ 3p^5\ 3d\ 4s$	$^2P_{1/2}$	837661	839279 (−1618)
62	$3s^2\ 3p^5\ 3d\ 4s$	$^4F_{9/2}$	–	844540
63	$3s^2\ 3p^5\ 3d\ 4s$	$^2P_{3/2}$	842829	844766 (−1937)
64	$3s^2\ 3p^5\ 3d\ 4s$	$^4F_{7/2}$	847145	847137 (8)
65	$3s^2\ 3p^5\ 3d\ 4s$	$^4F_{5/2}$	849899	849973 (−74)
66	$3s^2\ 3p^5\ 3d\ 4s$	$^4F_{3/2}$	852849	853003 (−154)
67	$3s^2\ 3p^5\ 3d\ 4s$	$^2F_{7/2}$	855100	856493 (−1393)
68	$3s^2\ 3p^5\ 3d\ 4s$	$^2F_{5/2}$	860615	862322 (−1707)
69	$3s^2\ 3p^5\ 3d\ 4s$	$^4D_{7/2}$	874711	878133 (−3422)
70	$3s^2\ 3p^6\ 5d$	$^2D_{3/2}$	–	878690
71	$3s^2\ 3p^6\ 5d$	$^2D_{5/2}$	–	878916
72	$3s^2\ 3p^5\ 3d\ 4s$	$^4D_{5/2}$	876765	880421 (−3656)
73	$3s^2\ 3p^5\ 3d\ 4s$	$^4D_{3/2}$	877476	881507 (−4031)
74	$3s^2\ 3p^5\ 3d\ 4s$	$^4D_{1/2}$	878264	882329 (−4065)
75	$3s^2\ 3p^5\ 3d\ 4s$	$^2D_{5/2}$	879021	884089 (−5068)
76	$3s^2\ 3p^5\ 3d\ 4s$	$^2D_{3/2}$	881345	886603 (−5258)
77	$3s^2\ 3p^5\ 3d\ 4s$	$^2F_{5/2}$	884331	888349 (−4018)
78	$3s^2\ 3p^5\ 3d\ 4s$	$^2F_{7/2}$	887325	890584 (−3259)
79	$3s^2\ 3p^5\ 3d\ 4s$	$^2D_{3/2}$	889113	893935 (−4822)
80	$3s^2\ 3p^5\ 3d\ 4s$	$^2D_{5/2}$	890845	895255 (−4410)
81	$3s^2\ 3p^6\ 5f$	$^2F_{5/2}$	927059	926655 (404)
82	$3s^2\ 3p^6\ 5f$	$^2F_{7/2}$	927102	926734 (368)
90	$3s^2\ 3p^6\ 6f$	$^2F_{5/2}$	1016560	1015284 (1276)
91	$3s^2\ 3p^6\ 6f$	$^2F_{7/2}$	1016570	1015322 (1248)
103	$3s^2\ 3p^6\ 7f$	$^2F_{5/2}$	1069873	1068877 (996)
104	$3s^2\ 3p^6\ 7f$	$^2F_{7/2}$	1070029	1068900 (1129)

Notes. The columns provide: the experimental level energies E_{exp} (cm^{-1}), those for the 23 configuration target (Table 5) E_{calc} (cm^{-1}). Values in parentheses indicate differences with the observed and theoretical energies. The full dataset is available at the CDS.

Table 7. List of strongest Fe VIII lines in the 50–170 Å range.

i–j	Levels	Int 10^8	Int 10^{12}	gf	$A_{ji}(s^{-1})$	λ_{exp}(Å)	λ_{th}(Å)
2–49	$3p^6 3d\ ^2D_{5/2}$–$3p^5 3d^2\ ^2D_{5/2}$	8.6	8.5	7.06	2.8×10^{11}	168.172	159.73 (-8.4)
1–50	$3p^6 3d\ ^2D_{3/2}$–$3p^5 3d^2\ ^2D_{3/2}$	6.1	5.0	4.56	2.7×10^{11}	167.486	159.20 (-8.3)
2–48	$3p^6 3d\ ^2D_{5/2}$–$3p^5 3d^2\ ^2P_{3/2}$	5.0	4.9	3.82	2.2×10^{11}	168.544	162.16 (-6.4)
1–47	$3p^6 3d\ ^2D_{3/2}$–$3p^5 3d^2\ ^2P_{1/2}$	3.1	2.5	2.10	2.4×10^{11}	168.929	162.43 (-6.5)
2–54	$3p^6 3d\ ^2D_{5/2}$–$3p^6 4f\ ^2F_{7/2}$	1.3	1.3	4.30	2.1×10^{11}	131.240	129.02 (-2.2)
1–53	$3p^6 3d\ ^2D_{3/2}$–$3p^6 4f\ ^2F_{5/2}$	1.0	0.82	2.97	1.9×10^{11}	130.941	128.71 (-2.2)
2–50	$3p^6 3d\ ^2D_{5/2}$–$3p^5 3d^2\ ^2D_{3/2}$	0.59	0.48	0.44	2.6×10^{10}	168.003	159.69 (-8.3)
1–49	$3p^6 3d\ ^2D_{3/2}$–$3p^5 3d^2\ ^2D_{5/2}$	0.52	0.52	0.43	1.7×10^{10}	167.654	159.24 (-8.4)
1–48	$3p^6 3d\ ^2D_{3/2}$–$3p^5 3d^2\ ^2P_{3/2}$	0.48	0.47	0.37	2.2×10^{10}	168.024	161.65 (-6.4)
2–84	$3p^6 3d\ ^2D_{5/2}$–$3p^6\ 5f\ ^2F_{7/2}$	0.20	0.20	1.40	9.9×10^{10}	108.077	108.13 (0.1)
1–83	$3p^6 3d\ ^2D_{3/2}$–$3p^6\ 5f\ ^2F_{5/2}$	0.16	0.13	0.98	9.3×10^{10}	107.868	107.92 (0.0)
2–53	$3p^6 3d\ ^2D_{5/2}$–$3p^6 4f\ ^2F_{5/2}$	7.3×10^{-2}	5.9×10^{-2}	0.22	1.4×10^{10}	131.257	129.03 (-2.2)
2–93	$3p^6 3d\ ^2D_{5/2}$–$3p^6\ 6f\ ^2F_{7/2}$	6.8×10^{-2}	6.6×10^{-2}	0.73	6.3×10^{10}	98.548	98.68 (0.1)
1–92	$3p^6 3d\ ^2D_{3/2}$–$3p^6\ 6f\ ^2F_{5/2}$	5.1×10^{-2}	4.2×10^{-2}	0.51	5.8×10^{10}	98.371	98.49 (0.1)
2–104	$3p^6 3d\ ^2D_{5/2}$–$3p^6\ 7f\ ^2F_{7/2}$	3.1×10^{-2}	3.0×10^{-2}	0.51	4.9×10^{10}	93.616	93.72 (0.1)
1–103	$3p^6 3d\ ^2D_{3/2}$–$3p^6\ 7f\ ^2F_{5/2}$	2.3×10^{-2}	1.9×10^{-2}	0.35	4.5×10^{10}	93.469	93.56 (0.1)

Notes. The relative intensities (photons) $Int = N_j A_{ji}/N_e$ are normalised to the strongest transition and were calculated at electron densities of 10^8 and 10^{12} cm^{-3} and log T[K] = 5.6. Weighted oscillator strengths gf and A-values (s^{-1}) are shown. Experimental λ_{exp} (Å) and theoretical λ_{th} (Å) wavelengths are included. Values in parentheses indicate differences between the observed and theoretical wavelengths.

Table 8. List of lines in the soft X-rays from quiet Sun observations.

Manson (1972)			Behring et al. (1972)		
Wavelength Å	Flux 10^6 ph cm^{-2} s^{-1}	ID	Wavelength Å		ID
93.02	3.8		93.206	15	
93.46	2.4		93.618	30	
93.71	3.1		93.838	20	
94.04	7.3	Fe X	93.933	20	
94.45	1.8		94.016	35	Fe X
94.95	1.6				
103.58	8.5	Fe IX			
108.00	2.2	Fe VIII			

5.1. Fe IX

The strongest line in the soft X-ray spectra is the 3p–4s $^1S_0$–$^1P_1$ 103.566 Å line, which we use as a reference. First, we note that the use of the R-matrix data in the Fe IX model ion means that the predicted intensity of this line is about twice that which is obtained when only DW data are used. The relative intensity of this line with e.g. the 3d–4f transitions suggests that we have about the correct theoretical intensity. The decay from the 4s $^3P_1$ 105.208 Å is predicted to have half the intensity of the 103.566 Å line at coronal densities, but actually in the solar spectrum the ratio is 0.7. This could be due to a blend, considering that at high densities the ratio increases to 0.6, closer to that which is observed (0.75, Lepson et al. 2002). The alternative is that level mixing is not accurate, although all of the different structure runs provide similar values for the radiative data.

Our ion model predicts several 3d–4f transitions to be strong. Some of them have not been previously identified. We tentatively identify two of them, observed both in solar and laboratory spectra. We assign them the 133.923 and 136.572 Å, and notice that identification of these lines with 3d–4f transitions was already suggested by Lepson et al. (2002) and also by Foster & Testa (2011). In addition, we identify the 116.803 Å as a self-blend. The decays from the 4d levels were identified by Alexander et al. (1965).

After the 3p–4d lines, we predict that the strongest transition array is the 3d–5f one. By comparing EBIT results with calculations using the Hebrew University Lawrence Livermore Atomic Code (HULLAC, Bar-Shalom et al. 2001) Lepson et al. (2002) suggested that there are a number of 5f–3d transitions around 90 Å, in particular three 5f–3d transitions at 91.98, 93.59 and 94.07 Å.

At low coronal densities, we find that only one line should be observable in the solar spectra, the 5–302 $3p^5\ 3d\ ^3F_4$–$3p^5\ 5f\ ^3G_5$. At high densities, there are a number of transitions which might become observable. We have searched for a correspondence between our theoretical energy splittings among the 5f levels and the difference in wavelengths provided by Lepson et al., and found a few possible coincidences. A tentative identification for these lines is provided in Table 9.

The strongest 3d–5f line would be at 91.98 Å and further blended with two other transitions. The predicted ratio of this line with our reference 3p–4s 103.566 Å line is in excellent agreement with the measurement from Lepson et al. (2002), as Table 9 shows. This is very encouraging. Two other coincidences have been found. Two self-blends contributing to the lines observed at 93.59 and 94.07 Å by Lepson et al. In these cases, the predicted intensities are only half of what was observed. In the solar case, the strongest 91.98 Å line provides only 1/3 of the observed intensity (assuming that our reference line, the 3p–4s 103.566 Å is not in itself blended in the solar spectrum). The other 3d–5f lines provide very little flux to the observed solar lines. This is not surprising, considering that most lines are noted as blended by Manson. Also, this of course does not mean that in particular conditions, where strong transition-region emission is present, these lines could not be providing a significant contribution to the 94 Å AIA channel.

We searched for a possible identification of the lines from the 3d–6f transition array, considering that at least one should be observable in the EBIT spectra, but could not find any suitable

Table 9. Relative intensities for Fe IX lines.

Ion	λ_{exp}(Å)	λ_{th}(Å)	R_{obs} (Manson 72)	R_{th} (10^8)	R_{obs} (Lepson 02)	R_{th} (10^{12})	Transition indices
Fe IX	91.98	87.61 + 87.77 + 87.94	0.6	0.21	0.25	0.27	5–302 + 6–305 + 7–308
Fe IX	93.59	89.10 + 89.30	0.36	0.03	0.25	0.13	11–318 + 12–319
Fe IX	94.07	89.56 + 89.68 + 89.75	0.85	0.07	0.30	0.14	8–311 + 10–316 + 9–308
Fe IX	103.566	98.08 (-5.5)	1.0	1.0	1.0	1.0	1–107

Notes. Experimental λ_{exp} (Å) and theoretical λ_{th} (Å) wavelengths are included. Observed intensities from Manson (1972) and Lepson (2002) expressed relative to the Fe IX $3p^6\ ^1S_0$–$3p^5\ 4s\ ^1P_1$ intensity are shown. Theoretical intensities at 10^8 cm^{-3} and at 10^{12} cm^{-3} expressed relative to the Fe IX $3p^6\ ^1S_0$–$3p^5\ 4s\ ^1P_1$ intensity are also included.

candidate. Further work is needed to identify these lines, as well as other ones such as the 3d–5p.

It is interesting to note that many of the strongest lines, even at relatively low densities (quiet Sun corona), are decays to metastable levels. Indeed, many of the transitions, including the strongest of the 3d–5f, are from levels which become mainly populated through excitation from a metastable one, and not from the ground state. For example, the intensity of the $3p^5\ 3d\ ^3F_4$–$3p^5\ 5f\ ^3G_5$ line becomes four times weaker if only the excitation from the ground state is included in the model.

We have compared our results for Fe IX with those presented by Foster & Testa (2011) at the same density and temperature values and have found that their results are in reasonable agreement with ours.

We compare the intensities of the 3d–4f lines using the intensities listed in Datla et al. (1975, first case), which included corrections due to optical depth effects. The plasma source was measured to have $N_e = 10^{16.07}$ cm^{-3} and log T_e[K] = 6.04. We make use of the "emissivity ratio" technique (see Del Zanna et al. 2004, for details), whereby the observed intensity of a line is divided by its emissivity:

$$F_{ji} = \frac{I_{ob}\ N_e\ C}{h\nu N_j(N_e, T_e)\ A_{ji}} \quad (1)$$

calculated at a fixed electron density N_e (in this case $10^{16.07}$ cm^{-3}) and plotted as a function of the temperature T_e. I_{ob} is the observed intensity in the line, h is Planck's constant, ν is the frequency of the line and N_j is the number density of the upper level j of the emitting ion. The scaling constant C is chosen so the curves are close to unity. The emissivity ratios (see Fig. 4) show good agreement to within ±30%, with one exception, between theory and experiment for the $3s^2\ 3p^6$–3d, $3s^2\ 3p^6$–4s, and 3d–4f transitions, thus giving us confidence in the reliability of the present calculations for the 4f levels.

5.2. Fe VIII

We compare the intensities of the 3d–4f, 3d–5f lines using the intensities listed in Datla et al. (1975, second case). The level populations are in the high density limit and therefore have no relative sensitivity to changes in electron density. As the relative variation in temperature is greater than that in density the emissivity ratio has been plotted as function of the temperature and not of the density. The emissivity ratios show very good agreement between theory and experiment to within ±20% for the 3d–3d, 3d–4f, and 3d–5f transitions, thus giving us confidence in the reliability of the present calculations for the 5f levels (see Fig. 5). The contribution of missing resonances in the collision strengths for levels $n \geq 5$ is in fact not expected to be large.

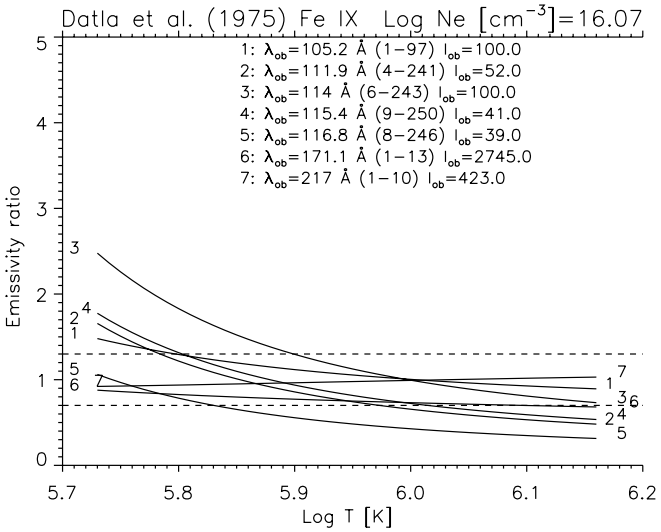

Fig. 4. The emissivity ratio curves from the calibrated theta-pinch laboratory spectra of Datla et al. (1975). I_{ob} indicates the measured line intensity. Dashed lines at ±30% have been added to give an indication of the agreement.

We then consider the 3d–5f, 3d–6f, 3d–7f transitions. Table 10 shows the relative intensities, predicted and observed. We find an excellent agreement between the relative ratios as observed in the laboratory by Ramonas & Ryabtsev (1980), which is very encouraging. We find some differences with the corresponding intensities predicted using the excitation data from Czyzak & Krueger (1966).

The two Fe VIII $3p^6\ 3d\ ^2D_{3/2}$–$3p^6\ 7f\ ^2F_{5/2}$ (93.56 Å) and $3p^6\ 3d\ ^2D_{5/2}$–$3p^6\ 7f\ ^2F_{7/2}$ (93.72 Å) transitions are within the SDO AIA 94 Å filter, together with the above Fe IX lines, and both the Fe XVIII (93.923 Å) transition from $2s\ 2p^6\ ^1S_{1/2}$–$2s^2\ 2p^5\ ^3P_{3/2}$ and the Fe X (94.012 Å) $3s^2\ 3p^4\ 4s\ ^2D_{5/2}$–$3s^2\ 3p^5\ ^2P_{3/2}$. Del Zanna et al. (2011) used the approximate excitation data from Czyzak & Krueger (1966), included in CHIANTI v6.0, to show that in particular conditions (at the footpoints of 1 MK loops) these 7f–3d lines are expected to provide a considerable contribution to the photons recorded in this band, so we can confirm here that to be the case. However, as Table 10 shows, there is plenty of unidentified flux in quiet Sun conditions, i.e. the 7f–3d transitions only provide a small fraction of the observed lines contributing to the 94 Å AIA channel.

6. Conclusions

The new atomic calculations presented here provide a significant advance over previous work. We have extended existing

Table 10. Relative intensities for Fe VIII lines.

Ion	λ_{exp}(Å)	R_{obs} (Manson 72)	R_{obs} (Ramonas & Ryabtsev 80)	R_{th} (10^8–10^{12})	Transition indices
Fe VIII	93.469	1.1	0.07	0.06	1–103
Fe VIII	93.616	1.4	0.09	0.09	2–104
Fe VIII	98.371 + 98.548	2.8	0.33	0.33	1–92 + 2–93
Fe VIII	107.868 + 108.077	1.0	1.0	1.0	1–83 + 2–84

Notes. Experimental wavelengths λ_{exp} (Å) are included. Observed intensities from Manson (1972) and Ramonas & Ryabtsev (1980) expressed relative to the combined Fe VIII 3d $^2D_{3/2}$–5f $^2F_{5/2}$ & 3d $^2D_{5/2}$–5f $^2F_{7/2}$ intensities are shown. Theoretical intensities at 10^8 cm^{-3} and 10^{12} cm^{-3} expressed relative to the combined Fe VIII 3d $^2D_{3/2}$–5f $^2F_{5/2}$ & 3d $^2D_{5/2}$–5f $^2F_{7/2}$ intensities are also included.

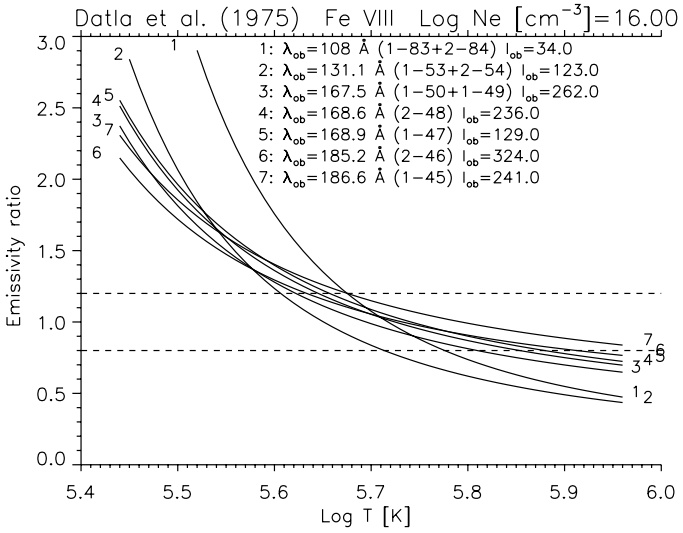

Fig. 5. The emissivity ratio curves from the calibrated theta-pinch laboratory spectra of Datla et al. (1975). I_{ob} indicates the measured line intensity. Dashed lines at ±20% have been added to give an indication of the agreement.

calculations of energy levels, radiative transition rates and collisional excitation rates up to $n = 6$ for Fe IX and $n = 7$ for Fe VIII. The new data allow the calculation of line intensities. We have provided several new identifications, but many other lines are still unknown.

This paper is just a first step into the complex area of identifying and providing atomic data for lines in the crowded 50–170 Å spectral region. Jordan (1968) used collisional excitation rates estimated by one of us (PJS) to suggest that e.g. for Fe IX transitions from $3p^5\ 4l$ (l = s, p, d, f) to either the ground state or the $3p^5$ 3d would contribute significantly to the observed lines. A large number of lines present in this region have yet to be identified, however we do find for some transitions a relatively good agreement with observations.

Based on our calculations the predicted contribution of Fe IX 5f–3d and Fe VIII 7f–3d transitions is only a small fraction of the observed lines in the 93–95 Å region for quiet Sun conditions. As a result the contribution of these lines to the SDO/AIA 94 Å filter is predicted to be small.

Acknowledgements. The authors thank Dr. Adam Foster & Dr. Paola Testa for providing their Fe IX atomic data for comparison with our own. The authors acknowledge the support of STFC. B.O.D. was supported by funding from the Gates Cambridge Trust. CHIANTI is a collaborative project involving researchers, at the Universities of: Cambridge (UK), George Mason (USA), and Michigan (USA). This work was carried out as part of the UK APAP project.

References

Aggarwal, K. M., Keenan, F. P., Kato, T., & Murakami, I. 2006, A&A, 460, 331
Alexander, E., Feldman, U., & Fraenkel, B. S. 1965, J. Opt. Soc. Am., 55, 650
Aschwanden, M. J., & Boerner, P. 2011, ApJ, in press
Badnell, N. R. 1997, J. Phys. B: At. Mol. Opt. Phys., 30, 1
Badnell, N. R. 2011, Comp. Phys. Commun., 182, 1528
Bar-Shalom, A., Klapisch, M., & Oreg, J. 2001, J. Quant. Spec. Radiat. Transf., 71, 169
Behring, W. E., Cohen, L., & Feldman, U. 1972, ApJ, 175, 493
Beiersdorfer, P., Lepson, J. K., Brown, G. V., et al. 1999, ApJ, 519, L185
Brinkman, A. C., Gunsing, C. J. T., Kaastra, J. S., et al. 2000, ApJ, 530, L111
Culhane, J. L., Harra, L. K., James, A. M., et al. 2007, Sol. Phys., 60
Czyzak, S. J., & Krueger, T. K. 1966, ApJ, 144, 381
Datla, R. U., Blaha, M., & Kunze, H.-J. 1975, Phys. Rev. A, 12, 1076
Del Zanna, G. 2009, A&A, 508, 513
Del Zanna, G., Berrington, K. A., & Mason, H. E. 2004, A&A, 422, 731
Del Zanna, G., O'Dwyer, B., & Mason, H. E. 2011, A&A, accepted
Dere, K. P., Landi, E., Young, P. R., et al. 2009, A&A, 498, 915
Eissner, W. 1998, Comp. Phys. Commun., 114, 295
Eissner, W., Jones, M., & Nussbaumer, H. 1974, Comp. Phys. Commun., 8, 270
Fawcett, B. C., Peacock, N. J., & Cowan, R. D. 1968, J. Phys. B: At. Mol. Phys., 1, 295
Fawcett, B. C., Kononov, E. Y., Hayes, R. W., & Cowan, R. D. 1972, J. Phys. B: At. Mol. Phys., 5, 1255
Foster, A. R., & Testa, P. 2011, ApJ, 740, L52
Gabriel, A. H., & Fawcett, B. C. 1965, Nature, 206, 390
Griffin, D. C., Pindzola, M. S., & Badnell, N. R. 2000, A&AS, 142, 317
Gu, M. F. 2003, ApJ, 582, 1241
Jordan, C. 1968, J. Phys. B: At. Mol. Phys., 1, 1004
Kruger, P. G., & Weissberg, S. G. 1937, Phys. Rev., 52, 314
Kruger, P. G., Weissberg, S. G., & Phillips, L. W. 1937, Phys. Rev., 51, 1090
Landi, E., & Young, P. R. 2009, ApJ, 707, 1191
Lemen, J., Title, A., Akin, D., et al. 2011, Sol. Phys., submitted
Lepson, J. K., Beiersdorfer, P., Brown, G. V., et al. 2002, ApJ, 578, 648
Liang, G. Y., & Badnell, N. R. 2011, A&A, 528, A69
Liang, G. Y., Badnell, N. R., Zhao, G., Zhong, J. Y., & Wang, F. L. 2011, A&A, 533, A87
Manson, J. E. 1972, Sol. Phys., 27, 107
O'Dwyer, B., Del Zanna, G., Mason, H. E., Weber, M. A., & Tripathi, D. 2010, A&A, 521, A21
Ramonas, A. A., & Ryabtsev, A. N. 1980, Optics and Spectroscopy, 48, 348
Storey, P. J., Zeippen, C. J., & Le Dourneuf, M. 2002, A&A, 394, 753
Summers, H. P. 2006, The ADAS User Manual v2.6, http://www.adas.ac.uk/manual.php
Verma, N., Jha, A. K. S., & Mohan, M. 2006, ApJS, 164, 297
Wagner, W. J., & House, L. L. 1971, ApJ, 166, 683
Woods, T. N., Eparvier, F. G., Hock, R., et al. 2010, Sol. Phys., DOI: 10.1007/S11207-009-9487-6
Young, P. R. 2009, ApJ, 691, L77
Young, P. R., & Landi, E. 2009, ApJ, 707, 173
Zeng, J., Jin, F., Zhao, G., & Yuan, J. 2003, J. Phys. B: At. Mol. Opt. Phys., 36, 3457